Optics Letters

Rapid prototyping of all-polymer AWGs for FBG readout using direct laser lithography

Elke Pichler,[1,*] Konrad Bethmann,[1] Christian Kelb,[2] and Wolfgang Schade[1,2]

[1]Technical University Clausthal, Institute of Energy Research and Physical Technologies, Am Stollen 19B, Goslar 38640, Germany
[2]Fraunhofer Institute for Telecommunications, Heinrich Hertz Institute, Fiber Optical Sensor Systems Department, Am Stollen 19H, Goslar 38640, Germany
*Corresponding author: elke.pichler@tu-clausthal.de

Received 1 August 2018; revised 28 September 2018; accepted 2 October 2018; posted 3 October 2018 (Doc. ID 341175); published 29 October 2018

This Letter describes the design, production, and characterization of a 1 × 2 arrayed waveguide grating (AWG) for fiber Bragg grating (FBG) readout, centered at 850 nm, with a channel spacing of 1 nm. The employed manufacturing process is laser direct lithography, a low-cost, rapid-prototyping capable, maskless method that allows for short iteration cycles and simple migration of a successful design to mask-based high throughput methods. We also consider the achievable AWG performance if used for strain or temperature measurements with FBG sensors.

https://doi.org/10.1364/OL.43.005347

Arrayed waveguide gratings (AWGs) are utilized in a multitude of applications, the most important one being wavelength-division multiplexing for optical communications [1]. Many applications in this field are centered on the telecom wavelength of $\lambda = 1550$ nm, where published work demonstrates devices manufactured from semiconductors [2], silicon-on-insulator [3], SiO_x on Si [4], and polymers [5–7]. Besides telecommunication applications, AWGs for the visible region are also used to determine the composition of chemical analytes [8] and can be found as a part of integrated photonic systems in microfluidics [9]. In particular, the processing of inorganic materials requires a fully equipped clean room, and setting up processes for integrated silicon photonic systems can easily cost several hundred thousand dollars [10]. The manufacturing of polymer-based integrated photonic systems skips several of the steps needed to process silicon-based devices, resulting in reduced prices for the setup and, especially for small batch sizes, a reduced price per unit. Typically, polymer-photonic systems consist of an organic or inorganic substrate layer, coated with a material that acts as the lower cladding for the core structures. In almost all cases, both the cladding and core are made from UV-curable polymers, which allow a patterning of the core structures by exposing the core resist through a patterned mask and, thus, transferring the desired structures. A following development step leaves the core material usually as ribs, which later fulfill the waveguide functionality. A final coating with the cladding material encloses the structures, shielding them from environmental influences such as moisture or mechanical damage and providing a defined refractive index step. However, even with the reduced number of steps, the process setup is cost-intensive. The manufacturing of the photo-mask, particularly, is highly expensive. This adds greatly to the overall cost of system development, since the mask also needs to be rebuilt with every iteration in the layout.

Maskless methods avoid this issue by generating arbitrary patterns from a digital design file without the need for costly mask generation. Projection lithography using beamshaping devices [11] and femtosecond direct writing [12] are two of the most prominent examples of maskless technologies. While the first method is more suited for the patterning of a small area up to one square millimeter, the latter generates waveguides in bulk material and is not comparable to conventional lithography methods.

For the design of integrated polymer-photonic systems, the laser direct lithography provides a process that is close to conventional lithography in most details, but replaces the mask-assisted exposure by a point-by-point exposure with a focused CW laser beam. Using laser direct lithography in the prototyping process results in faster iteration rates while reducing iteration costs significantly, making integrated polymer-photonic systems available for a wider range of applications. Furthermore, due to the inherent similarity between laser direct lithography and conventional lithography, a migration of the process to high-throughput methods is easily realizable, since most of the manufacturing steps are comparable.

In this Letter, we describe the use of direct laser lithography as a rapid-prototyping process for integrated optical systems applying a Heidelberg μPG 101 system. We designed, produced, and characterized AWGs for readout of fiber Bragg gratings (FBGs). We show that the devices, produced under low-cost circumstances, are suitable for interrogating FBGs at $\lambda = 850$ nm.

If the reflection spectrum of a sensing FBG is situated between two adjacent AWG channels as depicted in Fig. 1, the shift of the wavelength caused by elongation or temperature change of the sensing FBG can be interrogated by measuring the intensity P_1 and P_2 of the AWG channels, represented in the figure by the overlap between the FBG spectrum and the respective AWG channel spectra.

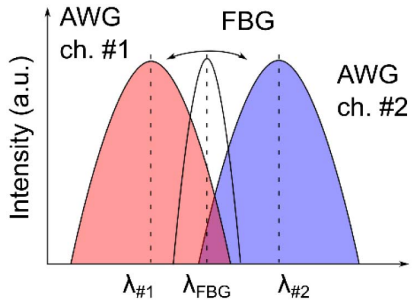

Fig. 1. Spectral overlap between AWG channels 1 and 2 and the FBG reflection spectrum.

The difference-over-sum ratio,

$$S = \frac{P_1 - P_2}{P_1 + P_2}, \tag{1}$$

with P_1 being the intensity measured at AWG output channel 1 and P_2 being the output intensity of channel 2. It can be shown that the ratio S just depends on the spectral profile of the reflected light of the sensing FBG and the transmitted spectrum of the AWG. Because both channels of the AWG are measured for the determination of the wavelength shift of the FBG, the interrogation system is immune against the uneven spectrum or power fluctuation of the light source [13].

The design of the waveguide dimensions and AWG geometry was performed with the commercial software EPIPPROP (Photon Design) under consideration of the refractive index data of the applied materials. The waveguide dimensions were chosen to be as small as possible, while still being reliably producible with laser direct lithography. Ultimately, this leads to few-mode behavior of the produced AWGs due to size limitations and, therefore, certain mode dispersion. Nonetheless, this design marks the compromise between repeatability in production and necessary sensibility for the target application.

To keep modal dispersion low, a relatively small grating order of $m = 40$ is chosen, as the dispersion decreases with decreasing optical path length difference between adjacent channels [14]. Simultaneously, a comparably long free propagation zone (FPZ) with $l = 4$ mm is used to increase the channel selectivity. The AWG device as shown in Fig. 4 is designed for a center wavelength of $\lambda_c = 850$ nm and a channel spacing of $\Delta\lambda = 0.7$ nm. It consists of 1 input waveguide that leads to a 1 to 50 star coupler (left FPZ), 50 arrayed waveguides, and a 50 to 2 star coupler (right FPZ). The radii of curvature for the star couplers and the arrayed waveguides are 2 and 1.5 mm, respectively. To avoid the detection of stray light, the input waveguide and the output waveguides are situated 90° to each other. The minimum radius of curvature for these waveguides is 3 mm. The simulated single-mode transmission spectrum for each output channel is shown in Fig. 2. A 188 μm thick cyclo-olefin polymer (COC) Zeonex flexible foil (http://microfluidic-chipshop.com, Jena) is used as a substrate for the AWG because of its high glass transition temperature of $T = 136$°C, good chemical resistance, and low water absorption rate of 0.1% per 24 h.

The AWG is realized as a buried waveguide structure (see Fig. 3) with the inorganic–organic copolymer system EpoCore/EpoClad (microresist technology, Germany) with negative

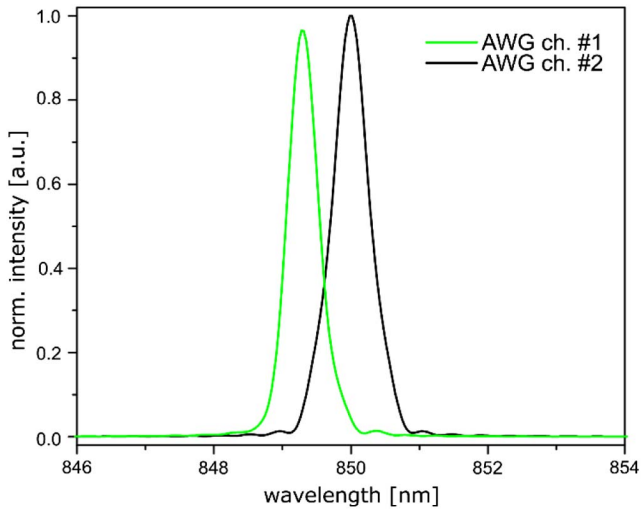

Fig. 2. Simulated transmission spectrum of the output waveguides for the fundamental mode of the designed AWG device.

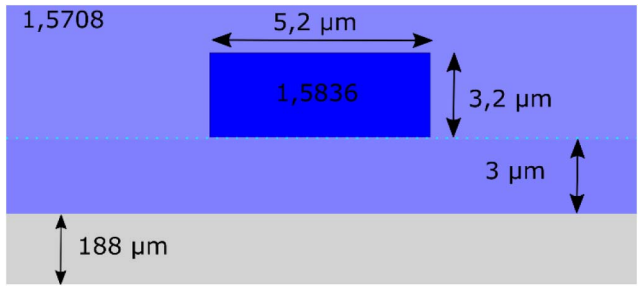

Fig. 3. Dimensions and refractive indices of the buried waveguides fabricated with the EpoCore/EpoClad material system.

resist behavior. The lower cladding consists of a 3 μm high EpoClad 2 layer. The waveguide core is fabricated from a 3.2 μm thick EpoCore 2 layer, which is patterned by laser direct lithography. The material of the upper cladding is EpoCore 20, a more viscous derivative of the lower cladding with the same refractive index. Figure 3 also shows the refractive indices of the used materials.

The refractive index difference between the core and cladding material is $\Delta n = 0.12$ at the used wavelength of 850 nm. The following procedure is applied for each of the three polymer layers: (1) treatment of the sample with oxygen plasma (Gala Instruments Plasma Prep) to increase the adhesion, (2) spin coating of the hybrid polymer, and (3) prebake of the spin coated layer to evaporate the residual solvent, (4) UV exposure to activate the photostarter in the monomer, (5) 30 min relaxation to reduce tensions in the layer, (6) post-exposure bake to crosslink the activated monomers, and (7) hardbake for 60 min at $T = 120$°C to improve the thermal stability of the resist. The fabrication of the cladding layers and core structure differs only in the applied UV-exposure technique: for upper and lower claddings, which are made of EpoClad, the whole layer is irradiated by a handheld UV lamp. The UV exposure of EpoCore for structuring the waveguides is done during the direct laser writing with a Heidelberg μPG 101 laser direct patterning (LDP) system. After exposure,

the sample is developed with mrDev600 (microresist technology, Berlin) to wash away unexposed areas. The LDP system uses a laser diode centered at $\lambda_c = 375$ nm with an output power of up to 70 mW for directly writing the pattern into the photoresist. While scanning the surface, the focus is automatically corrected. The smallest lateral dimensions of the produced device measure approximately 1 μm, resulting in a maximal aspect ratio of 3. The region in shown by the inset in Fig. 4. The distance between two phase-shifting waveguides is 6.2 μm center to center, resulting in a 1 μm gap where the highest aspect ratio occurs.

To characterize the AWG device, a temperature-controlled fiber optic alignment stage was used. The light of an superluminescent light emitting diode (SLED) source (EXS210037-01, optical power 2 mW, central wavelength of $\lambda_c = 840$ nm, 3 dB half-width: 47 μm, Exalos, Switzerland) is butt-coupled from a single-mode fiber [SM800 (5.6/125), NA, 0.1, Fibercore, UK] into the AWG. The light transmitted through each of the output waveguides was individually collected with a multimode fiber [MM (62.5/125), DRAKA] and measured with an optical spectrum analyzer (AQ6373B, Yokogawa, Japan).

According to the simulated design and using the described fabrication technique, AWG devices were realized and characterized. An example imaged with a confocal scanning microscope is shown in Fig. 5. Depicted is the junction between the right FPZ and the arrayed waveguides of the produced AWG device. The inset shows a higher magnification of the junction. It can be seen that small structures can be produced with satisfying precision, compared to the design file (see Fig. 4 and the corresponding inset). The most prominent problem for AWG devices manufactured with this technology is residual polymer in the gaps between the phase-hifting waveguides, either caused by backreflections from the transparent substrate material or by exceeding the resolution limits of the manufacturing process. By tuning both the exposure dose and design file accordingly, this issue could be avoided.

Faintly, the inset in Fig. 5 shows parallel stripes in the FPZ that are caused by the point-by-point manufacturing process. A metrological analysis shows these stripes as a ripple of approximately 30 nm peak-to-peak on the device surface. As this value is well below 1/10 of the operating wavelength of 850 nm and the device shows no significant limitation of function, no further effort was made to reduce or avoid this effect.

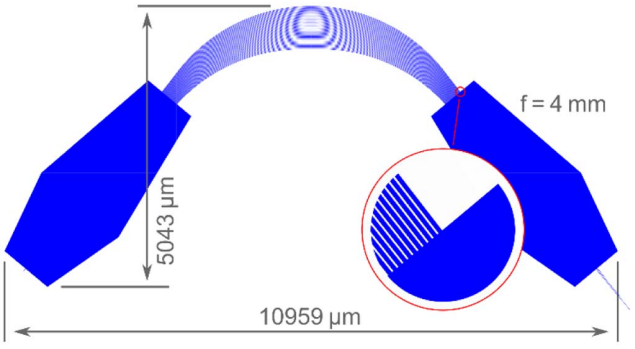

Fig. 4. Layout of the fabricated AWG device. The inlay shows the junction of the arrayed waveguides to the FPZ. The AWG device has one input waveguide and two output waveguides.

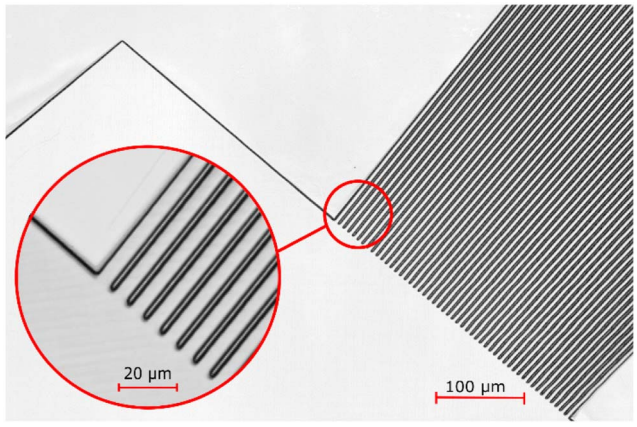

Fig. 5. Junction between the FPZ and the arrayed waveguides of the produced AWG device. The inset shows a higher magnification of the junction.

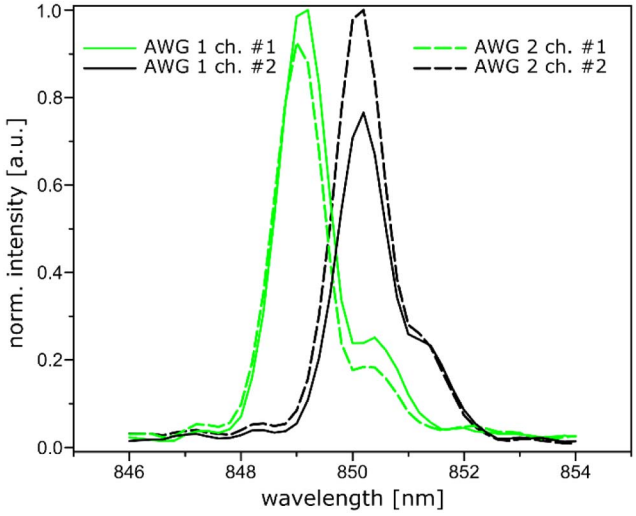

Fig. 6. Measured channel transmission spectra of two AWG devices.

Figure 6 shows the measured channel spectra of two individual AWGs. As can be seen, the design wavelengths are well met within a margin of error of 200 pm. The measurements were made at an ambient temperature of 24°C. The time between manufacturing of both AWGs was roughly 10 days. The derived characteristics of the devices are summarized and compared with the simulated results in Table 1. The FWHM and center wavelength were determined by fitting a Gauss function to the measured channel spectrum. Due to the broad emission spectrum of the SLED multiple, the refraction orders are detectable. The observed free spectral range of two adjacent orders is 19.4 nm for the order −1 and 20.4 nm for the order +1. Thus, for the application in connection with the narrow reflection spectrum of an FBG, crosstalk from other diffraction orders is not expected. The deviation of channel FWHM is in the range of 500 to 600 pm. This is mainly caused by the multimode behavior of the AWG waveguides, which leads to a broadening of the channel FWHM according to Kok *et al.* [14].

Table 1. Channel Properties of Two Manufactured AWGs in Comparison with the Simulated Values[a]

Simulation		Measured AWG 1		Measured AWG 2	
λ_c	FWHM	λ_c	FWHM	λ_c	FWHM
849.30	0.54	849.11	1.03	849.05	1.10
850.00	0.67	850.23	1.30	850.16	1.20

[a]All values are given in nm.

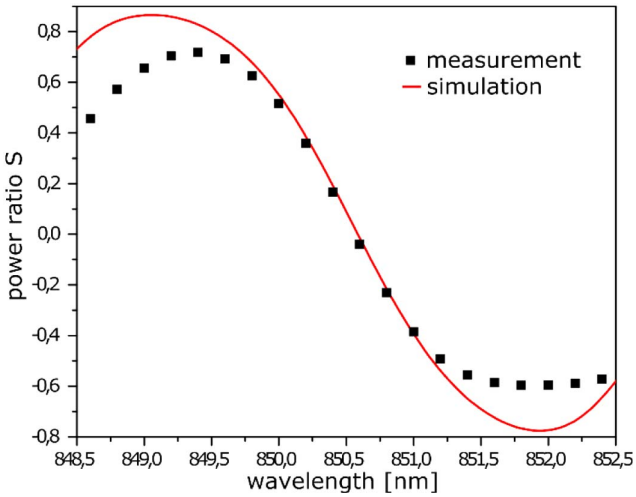

Fig. 7. Power ratio S calculated with measured spectral transmission functions of channel 1 and channel 2 of the AWG and the simulated FBG reflection spectrum, versus the wavelength (dotted line) to determine the corresponding wavelength shift of the FBG. The solid line gives the power ratio S calculated for the simulated AWG spectral transmission function and the simulated FBG refection spectrum.

The sensitivity of the all-polymer AWG device, depending on the shift of temperature, was measured to be −62 pm K^{-1}. This can be used to adjust the AWG spectra to fit even a slightly mismatching FBG by tuning the device temperature. Another possibility is to use two additional AWG channels to measure the device temperature with a second FBG and digitally compensate for the wavelength shift.

The feasibility of the produced AWG as an FBG interrogating device is estimated as depicted in Fig. 1. Modelling a hypothetical FBG reflection spectrum as a Gaussian function with a FWHM of 0.5 nm, the convolution of the measured AWG spectra with this Gaussian centered at a given wavelength yields the intensities that would be measured at the respective AWG channel.

The FWHM value in this case is based on values of typical FBG sensors, e.g., as described in Ref. [15]. Using Eq. (1), the difference-over-sum ratio S can be calculated for different wavelengths as shown in Fig. 7. A deviation from the theoretical s-curve due to the side lobes caused by the multimode behavior can be expected. However, compared to the ideal simulation, this only leads to a flattening of the curved part of the power ratio S (see Fig. 7), and has little effect on the linear part used for analysis and determination of the wavelength shift [16], apart from a restriction of the measurement range.

It can be seen that a shift of the sensing FBG can be measured in an interval of about $\Delta\lambda = 1.5$ nm. As shown in practical applications of the FBG for strain sensing [17], this wavelength shift equals a strain difference of 2200 μm/m for the FBG fiber used there.

Applied for temperature sensing, the FBGs in Ref. [17] exhibit a wavelength shift of 7.7 pm/K, corresponding to a theoretical measurable temperature change of up to 197 K. The sensitivity depends on the slope of the power ratio curve, while the resolution is mainly dependent on the resolution of the analog/digital converter used for readout of the photodiodes that would be detecting the two channel powers.

In conclusion, we presented, to the best of our knowledge, the first example of an all-polymer AWG fabricated by direct laser lithography. The AWG is centered at $\lambda_c = 850$ nm with a channel spacing of $\Delta\lambda = 0.7$ nm. The maskless direct writing allows an easy and quick alteration of the desired design, which makes the technique well suited for prototyping, thus reducing the manufacturing costs for small batches of AWG devices significantly. The AWG device is feasible for the interrogation of an FBG with wavelength shifts in the range of $\Delta\lambda = 1.5$ nm.

Funding. Bundesministerium für Wirtschaft und Energie (BMWi) (03ET6105A); Deutsche Forschungsgemeinschaft (DFG) (TRR123).

Acknowledgment. The authors thank Daniel Nedelcu for laboratory assistance.

REFERENCES

1. W. Bogaerts, S. K. Selvaraja, P. Dumon, J. Brouckaert, K. de Vos, D. van Thourhout, and R. Baets, IEEE J. Sel. Top. Quantum Electron. **16**, 33 (2010).
2. P. Pan, J. An, L. Wang, Y. Wu, Y. Wang, and X. Hu, J. Semicond. **33**, 74010 (2012).
3. P. Dumon, W. Bogaerts, D. van Thourhout, D. Taillaert, R. Baets, J. Wouters, S. Beckx, and P. Jaenen, Opt. Express **14**, 664 (2006).
4. H. Nishi, T. Tsuchizawa, R. Kou, H. Shinojima, T. Yamada, H. Kimura, Y. Ishikawa, K. Wada, and K. Yamada, Opt. Express **20**, 9312 (2012).
5. N. Keil, H. H. Yao, and C. Zawadzki, in *Optical Fiber Communication Conference and Exhibit* (2001).
6. C. Chen, H. Wang, L. Wang, X. Sun, F. Wang, and D. Zhang, Optik **125**, 521 (2014).
7. R. Orghici, K. Bethmann, U. Zywietz, C. Reinhardt, and W. Schade, Opt. Lett. **41**, 3940 (2016).
8. K. Kodate and Y. Komai, J. Opt. A **10**, 44011 (2008).
9. J. S. Kee, D. P. Poenar, P. Neužil, L. Yobaş, and Y. Chen, Opt. Express **18**, 21732 (2010).
10. M. Streshinsky, R. Ding, Y. Liu, A. Novack, C. Gallan, A. E.-J. Lim, P. G.-Q. Lo, T. Baehr-Jones, and M. Hochberg, Opt. Photon. News **24**(9), 32 (2013).
11. M. Rahlves, M. Rezem, K. Boroz, S. Schlangen, E. Reithmeier, and B. Roth, Opt. Express **23**, 3614 (2015).
12. W. M. Pätzold, C. Reinhardt, A. Demircan, and U. Morgner, Opt. Lett. **41**, 1269 (2016).
13. H. Su and X. G. Huang, Opt. Commun. **275**, 196 (2007).
14. A. A. M. Kok, S. Musa, M. Borreman, M. B. J. Diemeer, and A. Driessen, IEEE Region 8 EUROCON 2003. Computer as a Tool (2003).
15. J. Burgmeier, P. Funken, and W. Schade, Proc. SPIE **7753**, 775382 (2011).
16. J. Koch, M. Angelmahr, and W. Schade, Appl. Opt. **51**, 7718 (2012).
17. J. Meyer, A. Nedjalkov, A. Doering, M. Angelmahr, and W. Schade, Proc. SPIE **9480**, 94800Z (2015).